Computers and Geotechnics 108 (2019) 40–52

Contents lists available at ScienceDirect

Computers and Geotechnics

journal homepage: www.elsevier.com/locate/compgeo

Research Paper

Discrete numerical simulations of torpedo anchor installation in granular soils

Nan Zhang*, T. Matthew Evans

School of Civil and Construction Engineering, Oregon State Univ., 101 Kearney Hall, Corvallis, OR 97331, United States

ARTICLE INFO

Keywords:
Torpedo anchor
Anchor penetration
Discrete element modeling
Granular material
Microscopic

ABSTRACT

Torpedo anchors are a viable approach for mooring marine hydrokinetic (MHK) energy devices to the seafloor. These anchors can serve to maintain station and to provide the reaction force for an MHK device. The ability of the anchor to perform these duties is a strong function of its penetration depth during installation. This is a large-strain problem not amenable to typical continuum numerical approaches. In the current work, we propose that the discrete element method (DEM) is a more appropriate tool to investigate the shallow penetration of torpedo anchors in sands. The effects of anchor mass, impact velocity, and soil interparticle friction are considered in the DEM simulations. The relative maximum penetration depths for different penetration conditions are quantified and presented. Granular material response at the microscale during penetration are used to provide insight into system response. Energy dissipation in the assembly by both friction and collision at the particle scale are considered. Results show that anchor penetration increases approximately linearly with an increase in impact velocity or anchor weight. Penetration decreases with an increase in interparticle friction (i.e., soil strength). Observations of microscale behaviors and energy calculations are used to provide insight into overall system response.

1. Introduction

Dynamically penetrated anchors (DPA), also called “torpedo” or “rocket” anchors, are used for mooring deep water offshore facilities. They are typically constructed by a cone-tipped cylindrical steel pipe sections filled with concrete or scrap chain and have a pad eye at the top. DPAs are installed through the kinetic energy acquired during anchor free fall through the water. A mooring line is typically connected to the top of the anchor. The design of DPAs includes the estimation of embedment depth and holding capacities for both short- and long-term time periods. Existing design methods are based on results from experimental tests and numerical simulations. Physical experiments, including full-scale in-situ testing and small-scale centrifuge models, have been performed by many researchers (e.g., [1,6,11,17,21,28,30,31,34–36,40,42,43,45,65,66]. Most of these tests were performed in fine-grained soils. The influence of impact velocity on embedment depth is the primary performance metric considered in these studies. The influence of anchor weight on penetration depth is often considered. Results reported by previous researchers indicate that larger anchor impact velocities and anchor weights will result in deeper penetration and higher holding capacities. Anchor model shapes, especially nose shape, will also influence the anchor penetration depth. Anchor penetration relies on the anchor total energy: the sum of kinetic energy and potential energy of the torpedo anchor.

Relatively fewer experimental tests have been performed on anchor penetration in sandy soils. Medeiros et al. [32] report results from full-scale field tests at two sites off the Brazilian coast, one with sandy soils and the other with fine-grained soils. Richardson [42] performed experiments of anchor penetration into kaolinite, calcareous sand, and silica flour. Chow et al. [5] developed a novel dynamically-installed anchor into sands and investigated the installation and holding capacity behavior. Both studies found that the anchor penetration depth is much deeper for kaolinite than for silica flour. Projectile penetration tests on granular soils have been more widely reported, mostly in military applications with very high impact velocities ($\gtrsim$300 m/s) (e.g. [2,8,15,16,39,46,49,51,53,54,67]). Factors such as projectile nose shape, projectile weight, gravity, and projectile body shape were considered. Power relationships between projectile penetration depth and mass-area ratio have been reported. Penetration depth was found to decrease rapidly as projectile radius increases.

O’Beirne et al. [33] performed numerical analyses of offshore anchor behavior, comparing FEM results with field tests to investigate the response of soil to different load inclinations during pullout. Raie and Tassoulas [40] used computational fluid dynamics (CFD) to simulate

* Corresponding author.
E-mail address: zhangn@oregonstate.edu (N. Zhang).

https://doi.org/10.1016/j.compgeo.2018.12.013
Received 15 May 2018; Received in revised form 13 December 2018; Accepted 14 December 2018

soil behavior during anchor penetration by approximating the soil as a fluid. Numerical analyses of cone penetration tests (similar to the mechanics of DPA) in granular soils and crushable sands have also been performed (e.g., [7,68]), but these studies consider low-velocity penetrations and assembly behavior remains in the quasi-static regime. Analyses to investigate microscale soil performance in the vicinity of anchor penetration have not been fully reported previously. In the current work, DEM is employed to investigate the anchor penetration as dynamic impact simulations and the microscale response of DPAs in sandy soils.

The discrete element method (DEM) allows for the simulation of soils as a collection of individual particles and is increasingly being applied to a wide array of problems that involve granular materials in contact with geostructures (e.g., [12,14,18,20,29,56,62–64]). DEM models predict emergent behavior in particulate assemblies based on simulation of independent particle behaviors. DEM has been previously used to study shear bands in sand, including free-field shearing [13,19,25,61] and also granular-continuum interface shearing [15,26,27,57–59,69]. Overall, simulated material response from DEM simulations has been shown to be consistent with results from physical experiments for a variety of loading conditions [13,60].

Anchor installation is the first step for deploying an offshore anchor system. In the case of DPAs for marine hydrokinetic (MHK) energy generators, anchors serve to keep devices on station and as the reaction force necessary for energy generation. The holding capacity of the anchors must bear the tensile force from ocean waves transmitted by mooring lines. The soil-anchor interface shear force as well as the anchor weight play major roles on the anchor holding capacity. Typically, the deeper the embedment, the higher the holding capacity. The properties of the seabed soils and the anchor (e.g., anchor weight) combine to determine the holding capacity and allowable reaction force for a given anchor design. Much of the previous work on DPA has focused on FEM analyses, CFD analyses, and/or limit equilibrium solutions and are only applicable to clay sediments [31,33,36,40]. However, both approaches neglect much of the fundamental physics occurring at the anchor-soil interface or do not consider DPAs embedded in sandy soils. This work uses DEM simulations to evaluate the response of DPAs in granular soils at the microscale and compares simulation results to experiments from the literature.

2. Numerical analysis of torpedo anchor penetration

2.1. DEM model of torpedo anchor penetration

Prior studies of dynamically penetrated anchors and projectile penetration tests have focused on factors such as impact velocity, nose and shaft shape, and anchor/projectile weight and their influence on penetration depth. The simulations below focus on similar effects and the penetration depths at a small scale and explore the microscale responses during anchor penetration.

The geometry of the DEM model of the DPA installation is shown in Fig. 1. The assembly consists of a collection of polydisperse spheres intended to simulate sandy soil specimen and larger particles combined into a stick-like clump to simulate a DPA. The dimensions of the granular assembly are defined as functions of median particle size d_{50}. Fig. 1 shows a state when the DPA has already penetrated the granular assembly. Mass scaling, wherein particle size is increased artificially (e.g., [14,70], is employed to decrease simulation time by increasing the maximum stable timestep for the simulations. Specifically, model diameter (D_s) and height (H) can be expressed in terms of d_{50} as $D_s/d_{50} = 40$, and $H/d_{50} = 50$, respectively. The diameter of the DPA is $D_a = 4.2d_{50}$. Material parameters are selected from the published literature (e.g., [15,20,26,27,69]. Contact stiffness is calculated using the method presented by Potyondy and Cundall [38] with a magnitude of 10^7–10^8 N/m a ratio k_s/k_n between 2/3 and 1 [9]. The material and model parameters are shown in Table 1.

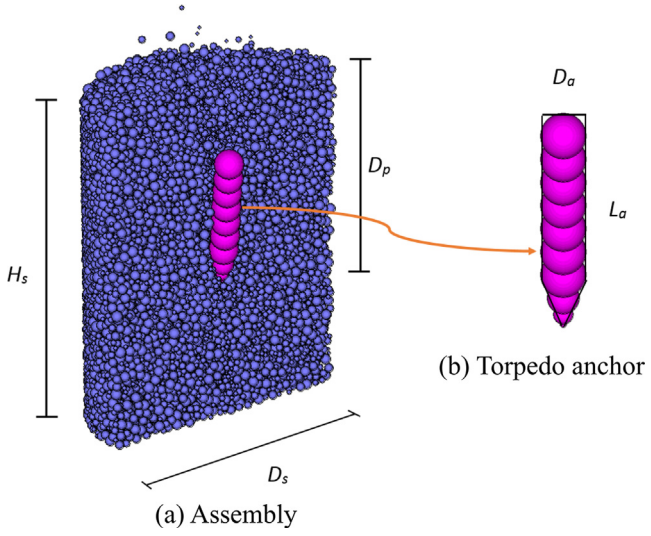

Fig. 1. DEM Model for torpedo anchor penetration.

Table 1
Material and model properties (baseline).

	Parameters	Value
Particles	Maximum diameter, d_{max} [m]	0.75
	Minimum diameter, d_{min} [m]	0.25
	Normal stiffness, k_n [N/m]	1×10^8
	Shear stiffness, k_s [N/m]	8×10^7
	Friction coefficient, μ [ ]	0.31
	Density, ρ_s [kg/m^3]	2650
Model	Height, H [d_{50}]	50
	Diameter, D_s [d_{50}]	40
	Initial porosity [ ]	0.426
DPA	Normal stiffness, k_{sn} [N/m]	1×10^8
	Shear stiffness, k_{ss} [N/m]	8×10^7
	Weight ratio, WR [ ]	3.77
	Diameter, D_a [d_{50}]	4.2

Anchor penetration is largely relying on the anchor total energy. Thus, a scaled gravity value is assigned for the simulation to balance the resultant gravitational force results from mass scaling and keep anchor total energy large enough for penetration, which is similar to centrifuge tests. The specimen is consolidated in the assigned gravity to equilibrium by cycling the granular assembly to a state where the average unbalanced contact force in the assembly is less than 1% of the average contact force. This as-consolidated void ratio can be adjusted by varying the particles' and walls' friction coefficients during consolidation, with a higher friction value resulting in a looser specimen. Note that $\mu_c \in [0, \mu]$ where μ_c is the friction coefficient used during consolidation and μ is the actual particle friction coefficient during anchor penetration. After consolidation, particle friction can be adjusted to assess the effects of particle friction on pullout resistance. Once the specimen is consolidated and equilibrated, the DPA is generated with the anchor tip immediately above the specimen and released by assigning a negative vertical constant velocity to simulate the impact velocity in practice.

According to Itasca [24], local damping is inappropriate for dynamic simulations (e.g., free flight of particles, particle impacts). Therefore, viscous damping is used to dissipate energy among the contacts in the simulations. Viscous damping ensures that the anchor is in free fall prior to impacting the granular soil. Viscous damping adds a dashpot at each contact in the normal and shear directions, which could provide forces that are proportional to the relative velocity between the two contacting entities [24]. Penetration is considered complete when the anchor vertical velocity is zero.

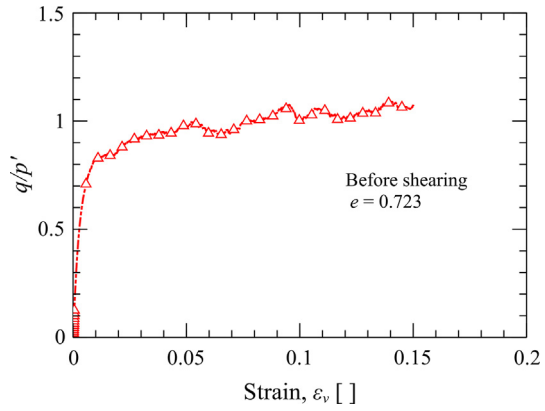

Fig. 2. Stress ratio of the granular assembly during triaxial shear.

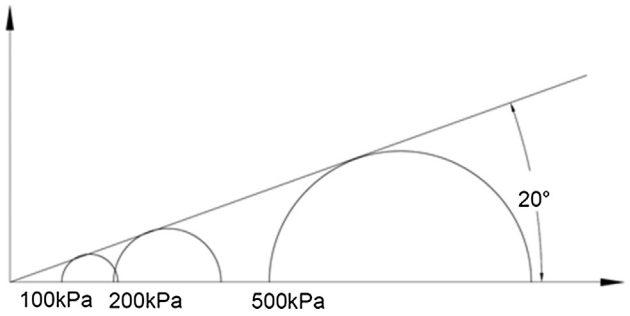

Fig. 3. Mohr's Circle of the granular assembly with same material properties shown in Table 1.

To assess the bulk properties of the simulated material, we modeled a triaxial compression test and present the results in Fig. 2. The assembly is sheared from a loose initial state (e = 0.723) and exhibits strain hardening behavior. Mohr's circles and a Mohr-Coulomb failure envelope for three triaxial compression tests are presented in Fig. 3.

2.2. Parametric studies

A series of parametric simulations has been performed to assess the effects of varying impact velocities on the maximum anchor penetration. Anchor impact velocity, anchor weight, and soil inter-particle friction are the parameters considered herein. These simulations serve two main purposes: (1) to elucidate problem physics by showing non-trivial variations in emergent response due to changes in physical inputs; and (2) to provide an intuitive check of overall model response – e.g., does anchor penetration depth increase with increasing impact velocities? – based on a high-level understanding of the physical system.

2.2.1. Impact velocity

In practice, torpedo anchors are released ~50–100 m above the seabed, resulting in an impact velocity of ~25–35 m/s. Impact velocities in this work range from 25 m/s to 40 m/s. Note that impact velocity is the velocity at the point that the torpedo anchor first impacts the seabed. In the current work, we compare penetration depth as a function of impact velocity from DEM simulations to experimental results reported in the literature and then use the model to investigate post-impact velocity profiles.

2.2.2. Anchor weight

Anchor penetration depth also depends on anchor weight [42]. Weight of torpedo anchors can be controlled by filling the anchors with materials of varying density, which is modeled in DEM by using different particle densities in the anchor clump. Six different anchor weights are considered here and are referenced to the density of the soil being penetrated. We define the weight ratio (WR) as the ratio of anchor weight to the anchor weight when the density is equal to the particle density. The WRs considered range from 1.00 to 4.53.

2.2.3. Soil interparticle friction

Torpedo anchor penetration is a function of the total anchor energy, including kinetic energy (mass, velocity) and potential energy (mass). Soil interparticle friction, μ_p, influences the frictional energy dissipation of the torpedo anchor [23]. The ultimate penetration depth will therefore be influenced by the interparticle friction. The interparticle friction values considered herein are 0.20, 0.25, 0.31, 0.35 and 0.40.

2.3. Results and discussion from parametric studies

Simulations results are presented from a macroscopic perspective in this section, showing the influence of anchor impact velocity, anchor weight, and interparticle friction on the ultimate anchor penetration and anchor efficiency. Anchor efficiency is defined as the ratio of maximum holding resistance (also known as anchor holding capacity) to anchor dry self-weight [42]:

$$E_f = \frac{F_V}{W} \tag{1}$$

where E_f is anchor efficiency, F_V is anchor holding capacity, and W is anchor dry self-weight.

2.3.1. Impact velocity: comparison with published experimental results

To assess overall model performance, we compare predicted penetration depth as a function of impact velocity to results from various experimental studies reported in the literature. The majority of reported results are from experiments performed in fine-grained soils with relatively fewer results reported for torpedo anchor penetration into granular soils. According to Ehlers et al. [11], for the same impact velocity, torpedo anchor penetration into sandy soil has a similar penetration depth as for over-consolidated (OC) clay. Penetration depths into normally consolidated (NC) clay are larger than into sandy soils or OC clay. The penetration depth of torpedo anchors into silty soils is generally the smallest. Fig. 5 shows comparisons between experiments and DEM simulations. The relative penetration depths of torpedo anchors into NC clays are appreciably larger than into sandy soils, OC clays, and silts. Richardson et al. [41] performed penetration tests into sandy soil using an impact velocity of 24 m/s. For our DEM simulations, when the impact velocity is 25 m/s, the relative penetration depth is approximately the same as the experimental results reported by Richardson et al. [41]. In general, the trend of penetration depth with impact velocity for OC clays, sands, and DEM simulations are very consistent and collectively well-fit by a straight line, as shown in Fig. 5. Relative penetration depth increases linearly with increasing impact velocity. Ultimately, this implies that the model, even when not calibrated to specific measurements, captures the basic problem physics well: i.e., it predicts penetration depths that are consistent with those observed in practice.

To further assess the effects of impact velocity on anchor behavior, we define shearing resistance during penetration, S, as the unbalanced force on the anchor divided by the anchor shaft surface area in contact with the granular assembly. Fig. 4 shows the shearing resistance profile of the anchor for different impact velocities. Results show that the impact velocity does not influence the shearing resistance gradient, which shows a constant rate of increase in resistance with increasing penetration depth. We expect that the granular assembly is partially drained during penetration. That anchor penetration into sandy soils is partially drained to undrained has been reported by White et al. [52]. We see from Fig. 4 that different impact velocities have similar shearing resistance gradients, indicating that strain rate effects in the simulated material are effectively constant for the range of impact velocities

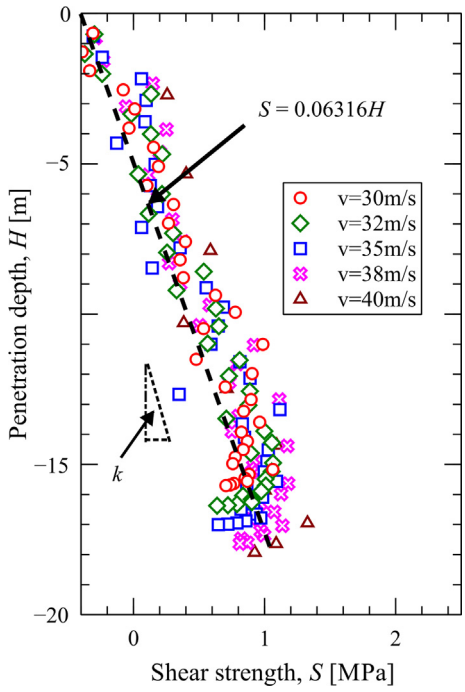

Fig. 4. Shear strength profiles with anchor penetration for different impact velocities.

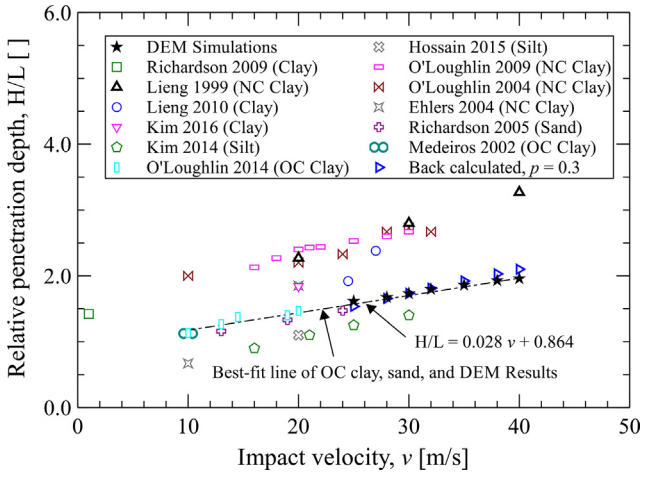

Fig. 5. Comparisons between experimental and DEM simulations.

considered. This observed shearing resistance gradient is analagous to the undrained shear strength gradient measured in clays from T-bar tests, as reported by Yun and Bransby [55].

The undrained shear strength gradient k in a granular assembly can be obtained from Fig. 4 using the method described by Yun and Bransby [55] for obtaining the value in clayey soil. Following Ehlers et al. [11], O'Loughlin et al. [36], and Hossain et al. [21], the total energy method is applied in this paper to evaluate the selection of anchor size according to anchor embedment depth. From analyzing experimental test data of torpedo anchor penetration on normally consolidated and overconsolidated clays, O'Loughlin et al. [36] and Hossain et al. [21] found a relationship between embedment depth and total energy that is expressed as follows:

$$\frac{z_e}{D_{eff}} \approx \left(\frac{E_{total}}{kD_{eff}^4}\right)^{1/p} \tag{2}$$

where D_{eff} is the effective diameter of the anchor cross section, z_e is tip

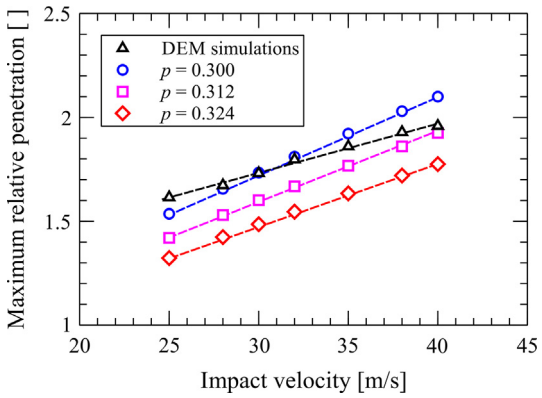

Fig. 6. Embedment depth obtained from back-calculation using the total energy method.

penetration depth, E_{total} is anchor total energy, k is the undrained shear strength gradient, p = 3 for overcosolidated clay and p = 3.24 for calcareous silt, as reported by O'Loughlin et al. [36] and Hossain et al. [21], respectively. Ehlers et al. [11] reports the anchor penetration into sandy soils has a similar penetration behavior as overconsolidated clay. The undrained shear strength gradient k is obtained from Fig. 4 as k = 63.16 kPa/m. Substituting k, E_{total}, and D_{eff} into Eq. (2), the calculated embedment depths with different p values are shown in Fig. 6. The maximum relative penetration depths obtained from back-calculation through total energy method are in the same range for overcosolidated clay (where p = 0.3) as the ones obtained from DEM simulation. Referring to Fig. 5, O'Loughlin et al. [37] have reported on anchor penetration with low impact velocities (v ≤ 20 m/s). The penetration depths for larger impact velocities may be obtained from the total energy method and are plotted in Figs. 5 and 6. In the simulations, we selected a viscous damping coefficient consistent with those reported in the literature (e.g., [4,10,22,50] and performed trial and error simulations to first test the penetration with low impact velocity (v = 20 m/s) and make sure DEM results reasonably agree with experimental results in the literature [37]. We then performed simulations with larger impact velocities (25–40 m/s) and compared the simulated values to back-calculated ones (Figs. 5 and 6) to confirm that system response was consistent with experimental observations across all strain rates being considered. The fraction of critical damping employed was 0.4, which corresponds to a coefficient of restitution of 0.25. The DEM simulations results are consistent with the predictions of Eq. (2).

In physical experiments, anchor dynamic penetration resistance at high impact velocities can be estimated from standard cone penetration test (CPT) measurements with an adjustment of the drainage condition [52]. The undrained shear strength can then be calculated from Eq. (3).

$$s_u = \frac{1}{2}p_f'\left(\frac{6\sin\phi_{cv}'}{3-\sin\phi_{cv}'}\right) \tag{3}$$

where p'_f is the mean stress at failure, ϕ'_{cv} is the critical state friction angle. The undrained penetration resistance is then calculated by multiplying undrained strength by a bearing factor N_{kt}. However, in DEM simulations, the undrained penetration resistance may be calculated directly by accumulating the contact shear forces between the anchor shaft and the contacting particles during penetration, which is also equal to the unbalanced force acting on the anchor.

2.3.2. Impact velocity: post-impact velocity profiles

Fig. 7 shows the velocity profile during anchor penetration for various impact velocities. Anchor velocity first increases and then decreases due to energy dissipation. The motion of anchor penetration into the seabed can be quantified using Newton's second law of motion and the force applied to the anchor during penetration [36]. According

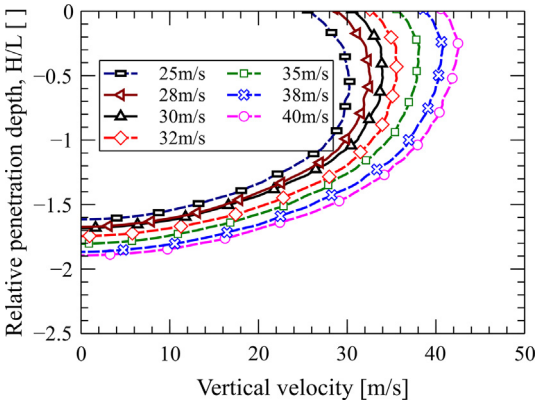

Fig. 7. Anchor velocity profile during penetration for different impact velocities.

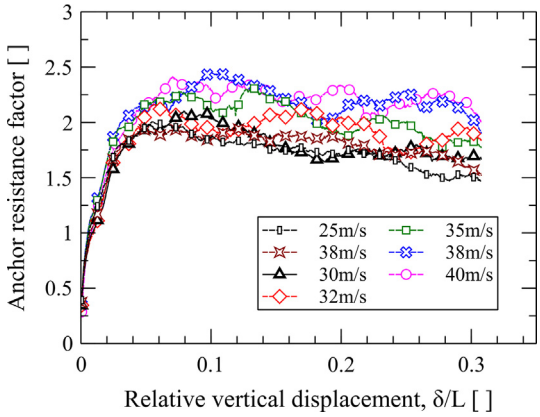

Fig. 9. Anchor resistance factor for different impact velocities.

to Fig. 4 and the discussion above, anchor impact velocity does not obviously influence the strength of the anchor-soil interface during penetration for the range of velocities considered. Anchor acceleration during penetration may be calculated by modifying an equation from O'Loughlin et al. [36] by setting the strain rate function equal to one, as shown in the following equation:

$$m\frac{d^2z}{dt^2} = W - F_b - F_{frict} - F_{bear} - F_d \tag{4}$$

where m is the anchor mass, z is the depth, t is time, W is the submerged anchor weight in water, F_b is the buoyant weight of the displaced soil, F_{frict} is frictional resistance, F_{bear} is bearing resistance, and F_d is inertial drag resistance. Eq. (4) describes the dynamic force equilibrium of anchor penetration. At the very beginning of anchor penetration, there is still a positive acceleration when the penetration starts. After first reaching a force balance (i.e., $\frac{d^2z}{dt^2} = 0$), the anchor will decelerate until reaching the ultimate penetration depth.

Fig. 7 shows that larger impact velocities result in deeper anchor penetration. The ultimate relative penetration depth, which is defined as the penetration depth normalized by anchor length, h/L (using the notation on the ordinate in Fig. 7) ranges from 1.6 when $v = 25m/s$ to 1.9 when$v = 40m/s$. These findings are generally consistent with results from physical experiments by Richardson [42], who reported the anchor tip penetration is 2.1–2.9 times the anchor length for impact velocities from 10 to 30 m/s. Fig. 8 shows the relationship between maximum relative penetration and impact velocity. Within the considered impact velocity range, maximum relative penetration increases approximately linearly with the increase of impact velocity. Chow et al. [5] reported that the penetration depth into loose sand is 38% deeper than into dense sand when the impact velocity is $v = 18.1$ m/s. When substituting the impact velocity into the best-fit equation, $H/L = 0.028v + 0.864$,the relative penetration depth is 1.368. In addition, when substituting impact velocity into silica sands reported in Richardson [42], the relative penetration depth is 1.67 which is much deeper than the experimental results (0.33–0.36). According to Figs. 2 and 3, the granular assembly in the paper is very loose with an internal friction angle of$\phi^{'} = 20$Â°. However, the silica sand used in the centrifuge test reported by Richardson [42] is very dense with an internal friction angle of $\phi^{'} = 42.8$Â° and a dilation angle $\psi^{'} = 5.3$Â°.

Once the anchor is embedded and the granular assembly has reconsolidated, the torpedo anchor will behave similarly to an anchor shaft. Fig. 9 shows anchor pullout behavior: specifically, anchor resistance factor, which is defined as the ratio of anchor resistance to anchor weight, versus relative vertical displacement for anchors embedded with different impact velocities. During anchor pullout, a very small upward velocity is applied to the anchor to simulate quasi-static strain-controlled pullout. The occurrence of a well-defined peak value is due to the volumetric particle redistribution, i.e. dilation, and is only clearly observed for the lowest impact velocity, which has the lowest penetration depth, and thus, the lowest confining stress and the least suppression of dilation. Anchor efficiencies are shown in Fig. 10. Anchor efficiency is used to assess performance and, in this work, was found to range from 2.1 to 2.6. O'Loughlin et al. [34] performed experimental tests on deep penetrating anchors having three different geometries. One of them had no flukes, similar to the anchor model used in our simulations. In their experiments, the anchor efficiency ranged from 1.7 to 3.6 for an average impact velocity of 23.5 m/s. Richardson [42] performed centrifuge tests to assess the influence of impact velocity on penetration depth and anchor efficiency. For impact velocities from 0 to 30 m/s, anchor efficiency varied from 1.2 to 3.2. Anchor efficiencies calculated from DEM simulations lie in the range of 1.9–2.6 for penetration velocities from 25 m/s to 40 m/s, which is

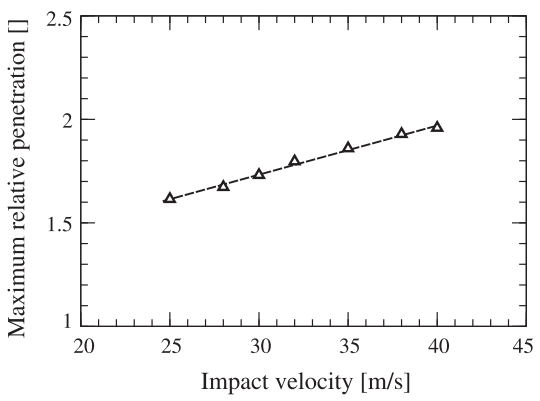

Fig. 8. Maximum relative anchor penetration under different impact velocities.

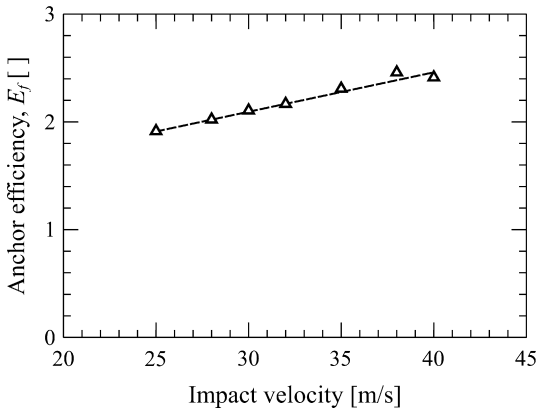

Fig. 10. Anchor efficiency for different impact velocities.

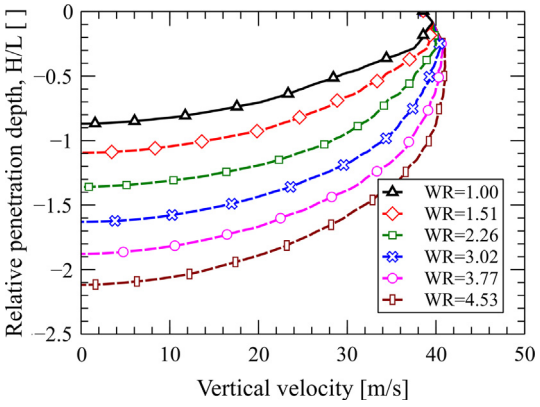

Fig. 11. Anchor velocity profile during penetration for different anchor weights (v = 38 m/s).

consistent with those from full-scale and model tests reported in the literature.

2.3.3. Anchor weight

Another parameter that influences anchor penetration behavior is anchor weight. Anchor weight varies linearly with anchor weight if anchor volume is constant. Fig. 11 shows the anchor velocity profile versus penetration for different anchor weights at an impact velocity of 38 m/s. The kinetic energy of the anchor is $E_K = \frac{1}{2}mv^2$, where m is anchor mass and v is the impact velocity. Thus, kinetic energy is linearly related to anchor mass. According to Eq. (2), when the weight ratio is smaller, the anchor will not accelerate as much as that for a larger weight ratio. In other words, a lighter anchor will decelerate more rapidly after impact due to rapid energy dissipation. Fig. 12 shows the relationship of maximum relative penetration depth as a function of anchor weight ratio, η, which is defined as the ratio of anchor density to the particle density of the granular assembly. Results show that penetration depth is linearly related to the anchor weight.

Fig. 13 shows the relationship between anchor efficiency and weight ratio. A bilinear relationship between anchor weight and anchor efficiency is apparent. Once anchor weight reaches a critical value, anchor efficiency remains constant for increasing weight ratios. Prior to the critical anchor weight ratio, anchor efficiency increases linearly with weight ratio. Anchor efficiencies range from 1.6 to 2.5.

2.4. Soil interparticle friction

Soil interparticle friction is another factor that influences the energy dissipation and thus the anchor penetration depth. Five different

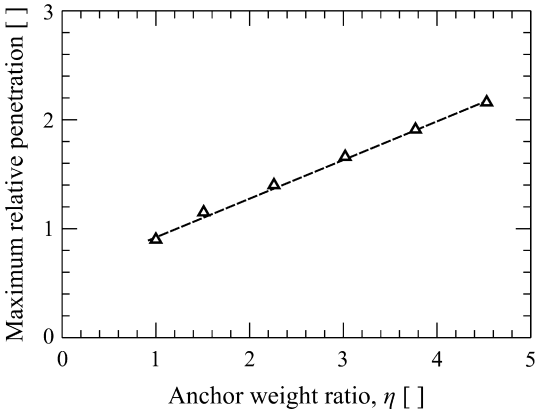

Fig. 12. Maximum relative penetration depths for different anchor weights (v = 38 m/s).

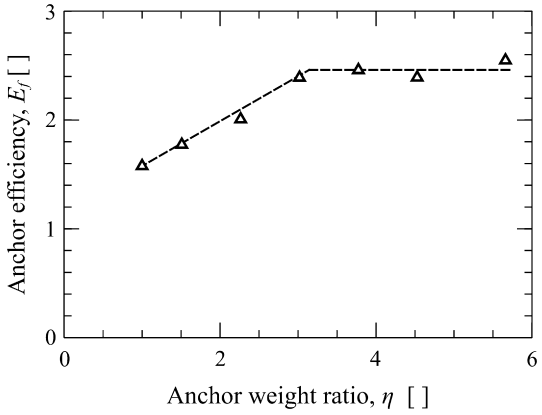

Fig. 13. Anchor efficiency for different weight ratios (v = 38 m/s).

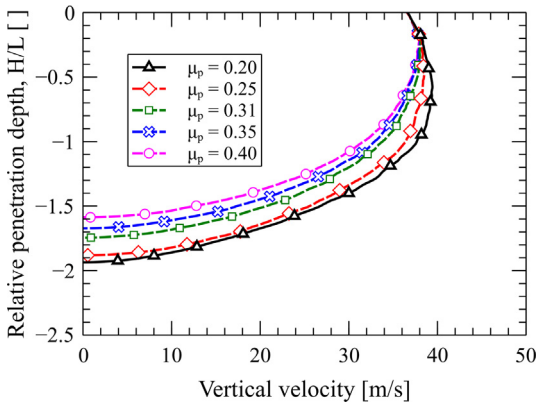

Fig. 14. Anchor velocity profile during penetration under different interparticle friction (v = 35 m/s).

interparticle frictions are considered in the simulations in the paper. Fig. 14 shows the velocity profile during anchor penetration under different interparticle frictions. Results have been found that the larger the interparticle friction, the faster the anchor will decelerate. According to Eq. (2), the friction resistance is correlated to interparticle friction. Anchor penetrated in assembly with larger interparticle friction turns to have larger friction resistance. Anchor turns to accelerate when interparticle friction is smaller. However, anchor will decelerate when penetration starts under larger interparticle frictions. Maximum relative penetration depth is found to decrease with the increase of interparticle friction (Fig. 15).

Fig. 16 shows anchor efficiencies for different values of interparticle

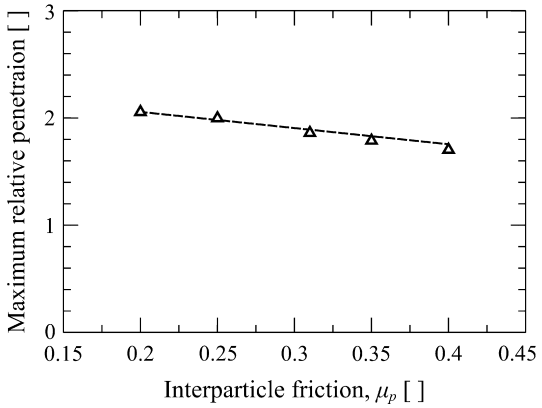

Fig. 15. Maximum relative penetration for different interparticle frictions (v = 35 m/s).

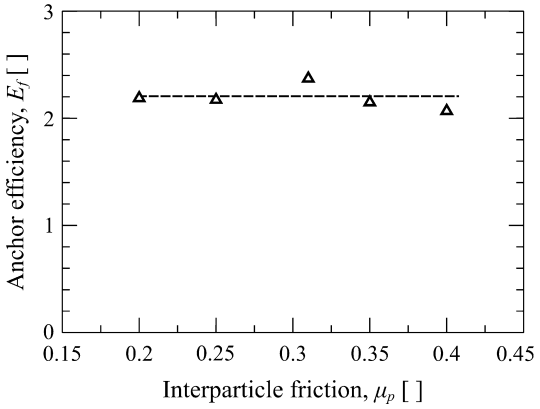

Fig. 16. Anchor efficiency under different interparticle frictions (v = 35 m/s).

friction. Although penetration depth decreases with an increase in interparticle friction, anchor efficiency remains essentially constant at ~2.2. Larger interparticle friction not only increases the frictional energy dissipation rate during penetration, but also the mobilized resistance along the anchor-soil interface. Thus, anchor efficiency does not decrease with the decrease in penetration depth.

3. Micromechanical investigation

Observed anchor installation and pullout behavior is a macroscale manifestation of microscale processes in the granular mass and at grain-anchor contacts. To facilitate interpretation of the macroscale responses presented above, microscale metrics such as anisotropy of fabric, mechanical coordination number and energy dissipation may be used to elucidate the installation behaviors. For the microscale investigations, the granular assembly is divided into four concentric subzones surrounding the torpedo anchor. Fig. 17 shows the subzones in the granular assembly between the boundary wall and torpedo anchor. Micromechanical behaviors within each subzone are investigated to assess the influence of anchor installation on the surrounding grains.

3.1. Fabric anisotropy

In soils, three types of fabric anisotropy are present due to deposition, changes in stresses, and geological stress history [71,72]: inherent, induced, and initial anisotropy. Anisotropy can be quantified considering particle orientations and branch vectors and can be determined from the second-order fabric tensor, given as Eq. (5):

$$\Phi_{ij} = \frac{1}{N_c}\sum_{k=1}^{N_c} n_i^k n_j^k \tag{5}$$

where n_i^k is the unit vector describing contact normal orientation for the k^{th} particle and N_c is the number of contacts in the assembly. The fabric tensor is a scalar measure of the directional distribution of

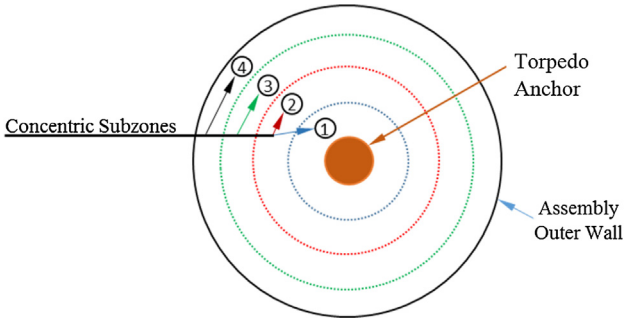

Fig. 17. Concentric subzones between the torpedo anchor and cylinder wall.

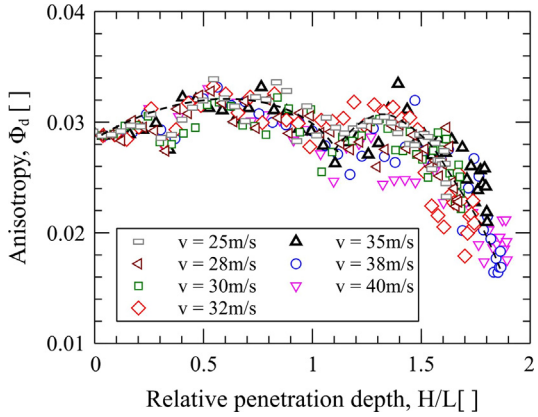

Fig. 18. Fabric anisotropy in the upper 60% of Zone-01 during anchor penetration for different impact velocities.

contact normal vectors. After computing the fabric tensor, the orientations and magnitudes of the anisotropy can be calculated. Three principal fabric parameters can be obtained via eigenvalue analysis of the fabric tensor. The major fabric parameter is Φ_1, the intermediate fabric parameter is Φ_2 and the minor fabric parameter is Φ_3. The anisotropy (or, deviator fabric) may be quantified using the three principal fabric parameters as Eq. (6):

$$\Phi_d = \frac{1}{\sqrt{2}}\sqrt{(\Phi_1 - \Phi_2)^2 + (\Phi_2 - \Phi_3)^2 + (\Phi_1 - \Phi_3)^2} \tag{6}$$

where $\Phi_d$is anisotropy or deviator fabric.

Figs. 18–20 show the fabric anisotropy in the upper 60% of Zone-01 during anchor installation for different impact velocities, different weight ratios, and different interparticle frictions, respectively. Dashed lines show the trend in anisotropy evolution. Fabric anisotropy in Zone-01 is found to initially increase and then decrease as the anchor moves through the soil profile for all impact velocities considered. A similar trend is observed for anisotropy evolution in Zone-01 for different anchor weights. This phenomenon may be explained as follows: at the beginning of penetration, particles are disturbed by the anchor via mechanisms such as contact loss and an increased velocity. Thus, the fabric tensor will change, as does the deviator fabric. The granular assembly becomes more chaotic as it is disturbed by the anchor and particles begin to interact dynamically. However, near the end of penetration, the particles have begun consolidating under gravity toward a more stable arrangement. The granular assembly at the end of penetration is more stable than prior to anchor penetration due to densification in the vicinity of the anchor. Finally, at equilibrium there is a large number of particles in contact with the anchor and these contact

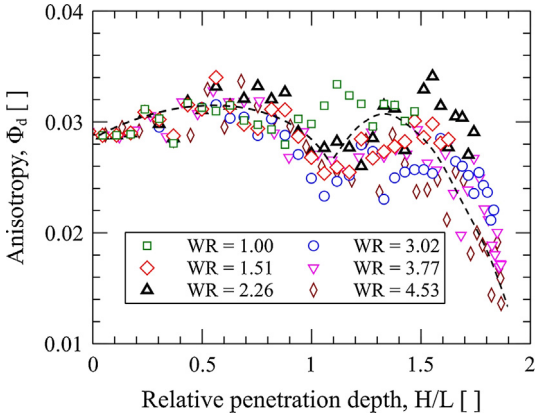

Fig. 19. Fabric anisotropy in the upper 60% of Zone-01 during anchor penetration for different anchor weight ratios.

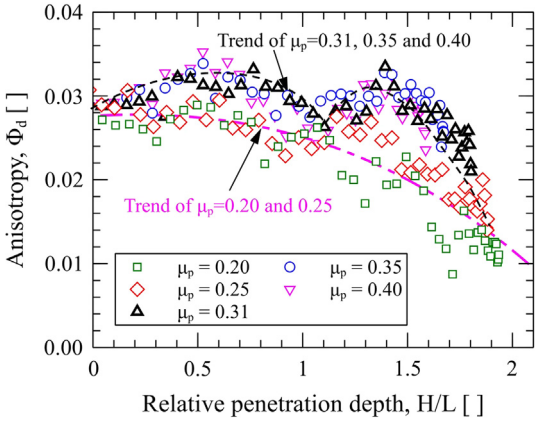

Fig. 20. Fabric anisotropy in the upper 60% of Zone-01 during anchor penetration for different inter-particle frictions.

orientations will effectively offset one another due to the axisymmetry of the problem, which results in decreased anisotropy.

Fig. 20 shows that if the interparticle friction is small (e.g. $\mu = 0.20 - 0.25$),there is no initial increase in the fabric anisotropy in Zone-01. Rather, anisotropy decreases monotonically from the first point of penetration. Immediately after the penetration is initiated, the different stress conditions on the longitudinal axis of the cylindrical sample volume and the boundary wall cause a stress gradient to be established. These stress gradients induce fabric gradients within the assemblies. Since each of the granular assemblies has the same dimensions, the inflection points for each of the simulations shown in Figs. 18–20 are the same ($\approx 1.1L$).

Evolution of fabric anisotropy can be better understood through observation of Fig. 21, which presents the average particle velocity in Zone 01 during anchor penetration. Results show that for interparticle frictions greater than the particle-anchor friction, particle velocities show an oscillating increasing-decreasing trend. There are valleys between two extreme points for each interparticle friction. At beginning of penetration, the anchor supplies kinetic energy to the particle assembly, disturbing the initial equilibrium. As the penetration continues, particle speeds increase, leading to greater disorder in the granular assembly and thus, increased fabric anisotropy. Due to gravitational damping and kinetic energy dissipation through frictional sliding and particle collisions, particle speeds decrease, shear forces accumulate at particle contacts, and the assembly tends towards stability, resulting in decreased fabric anisotropy. However, these shear forces cannot be infinitely accumulated as anchor penetration continues, so contacts will dissolve, particle speeds will thus increase, and so does the fabric

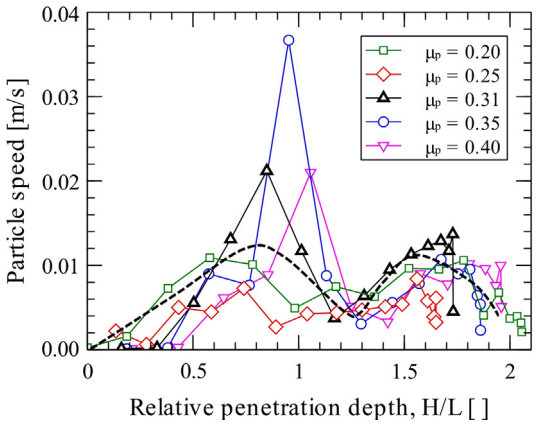

Fig. 21. Average particle speed of Zone 01 during anchor penetration for different interparticle frictions.

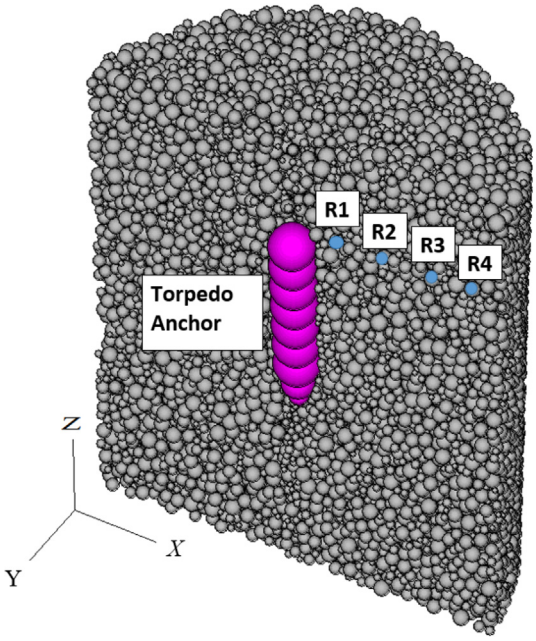

Fig. 22. Selected particles monitored during anchor penetration.

anisotropy. As the anchor energy dissipates, the granular assembly ultimately moves towards stability. This is the reason that Figs. 18–20 show increasing-decreasing-increasing-decreasing trends in fabric anisotropy.

In order to show the influences of anchor penetration on the surrounding particles, one particle in each subzone (Fig. 22) was monitored during penetration. The particles (R1-R4) have the same x and z coordinates and varying y coordinates; the z coordinate corresponds to a relative penetration of 0.513. Fig. 23 shows the x, y, and z components of particle velocities. This figure clearly shows a zone of disturbance in front of the tip of the anchor. The x velocities of particles R1, R2, and R3 increase at relative penetration depths of 0.20, 0.20, and 0.30, respectively, indicating the radial propagation of stress waves during penetration. Particle R4 is largely undisturbed, implying that the model domain is appropriately sized. As the penetration continues, the particles collapse inward behind the anchor. For the z-component of the velocity of R1, the negative value implies that particle is squeezed downward due to increasing stress and then heaved upward as that stress is relieved.

3.2. Mechanical coordination number and porosity

Here we use the coordination number to quantify particulate fabric. Coordination number, Z, is the number of contacts per particle in the material and is a measure of packing density and fabric connectivity at the particle scale. Coordination number is normally calculated using $Z = 2N_C/N_P$, where N_C is the number of contacts and N_P is the number of particles in the assembly [47,48]. However, due to numerical vibrations and the fully dynamic nature of DEM simulations, there will always be particles with only zero or one contact which do not contribute to force transmission in the system. Mechanical coordination number was thus defined as [48]:

$$Z_m = \frac{2N_c - N_1}{N_P - N_0 - N_1} \tag{7}$$

where N_1, N_0 are the numbers of particles with either one and zero contacts, respectively, and other terms are as previously defined.

Fig. 24 shows the mechanical coordination number of Zone-01 during anchor penetration for different impact velocities. Mechanical coordination numbers for all impact velocities considered experience a

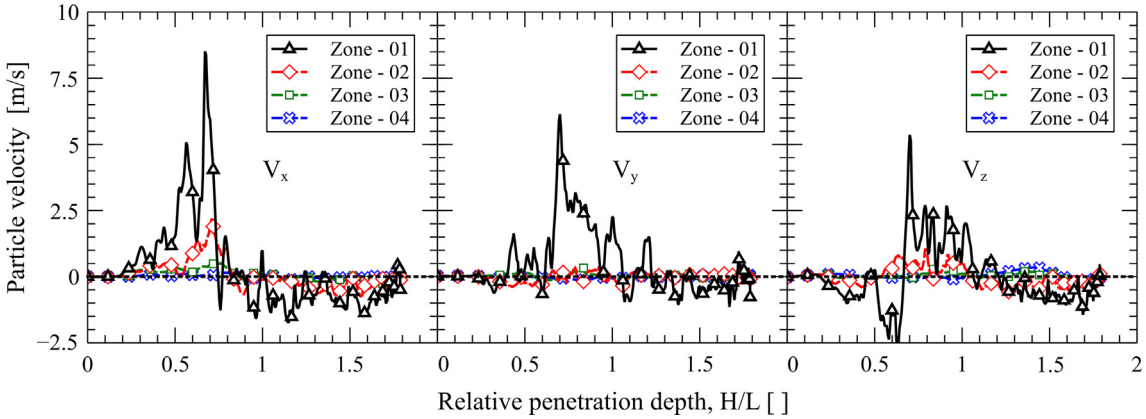

Fig. 23. x, y, and z velocities of selected particles.

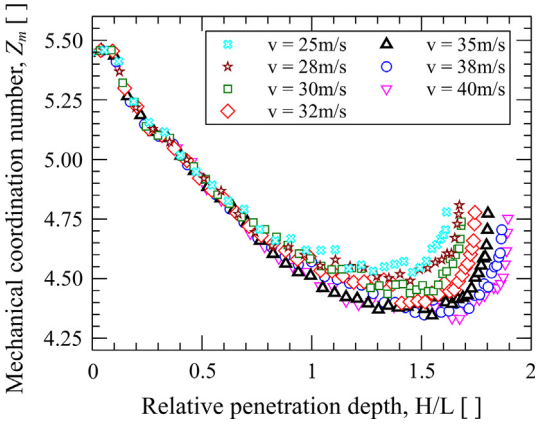

Fig. 24. Mechanical coordination number of Zone-01 during anchor penetration for different impact velocities.

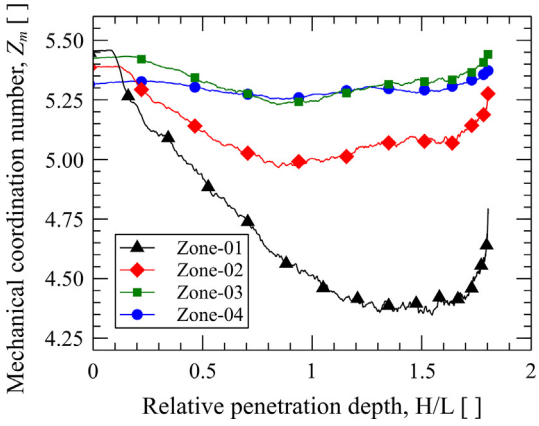

Fig. 25. Mechanical coordination number during anchor penetration for different subzones (v = 35 m/s).

rapid drop from approximately 5.45 at the beginning to a minimum of 4.25–4.50 and then ultimately increase to approximately 4.75 as the anchor comes to rest. That the mecahnical coordination number does not return to its pre-impact value is an indication of the disruptive effects of intruder penetration. Mechanical coordination numbers in Zone-01 reach their minimum when the relative penetration depth is in the range 1.4–1.6 and increases thereafter as the system calms and settles back in to a stable arrangement. As the anchor penetrates the assembly, its velocity is decreasing. Thus, kinetic energy is decreasing. Anchor potential energy is also decreasing as the anchor distance above some logical datum (e.g., the base of the assembly) decreases. Therefore, total anchor energy is decreasing until it is too small to continue inducing contact slip in the surrounding assembly. Anchor penetration–induced contact losses in Zone-01 are significant. During the early stages of penetration, the change in mechanical coordination number across the considered impact velocities is quite consistent. However, lower-velocity anchors reach a minimum mechanical coordination number at smaller penetration depths relative to higher-velocity anchors; this minimum value is also found to have an inverse relationship to penetration velocity, indicating greater overall disturbance for higher impact velocities.

Considering the influence of anchor penetration on the granular material in the different concentric subzones shown in Fig. 17, larger contact loss should occur closer to the penetrator. Fig. 25 shows the mechanical coordination number evolution in each of the four subzones for an impact velocity equal to 35 m/s. Mechanical coordination number in Zone-01 decreases sharply from 5.45 to 4.35 and then increases to approximately 4.80. Contacts are lost due to anchor impact and tend to re-form once anchor total energy is too small to cause shear failure at contact points until the anchor kinetic energy is zero (end of penetration). Anchor installation does not cause significant contact loss in the outer subzones, as evidenced by the relatively constant mechanical coordination numbers in Zone-03 and Zone-04.

Fig. 26 shows the porosities in each subzone during anchor penetration. Porosity in Zone-01 increases first from 0.395 to a peak value of 0.48 and then decreases to 0.43 at the end of penetration. The relative penetration depth where peak porosity occurs in Zone-01 corresponds to the depth where mechanical coordination number reaches a minimum (Fig. 25). Porosities in Zone-02, Zone-03, and Zone-04 decrease slightly due to the densification effects of anchor installation.

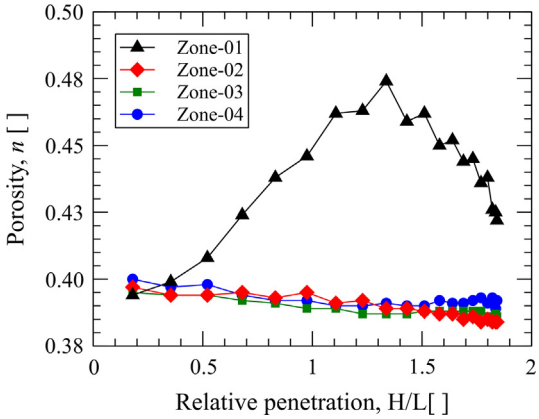

Fig. 26. Porosities during anchor penetration for different subzones (v = 35 m/s).

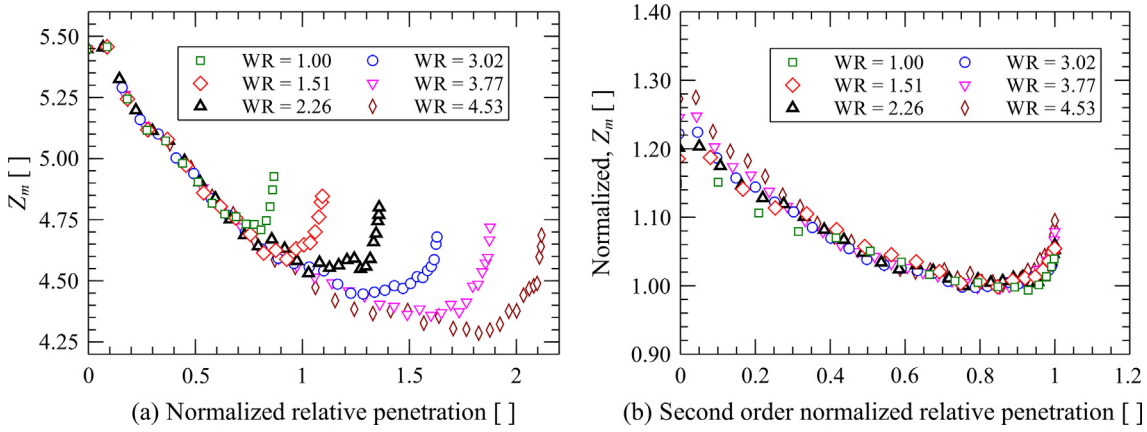

Fig. 27. Mechanical coordination number of Zone-01 during anchor penetration for different anchor weights (v = 38 m/s); (a) absolute response; and (b) normalized response.

Fig. 27 shows the mechanical coordination number evolution during anchor penetration for different anchor weights. As described above, anchor total energy will increase with increasing anchor weight. The mechanical coordination number changes shown in Fig. 27(a) are clearly a function of anchor weight. The larger the anchor weight, the larger the decrease in mechanical coordination number, indicating that larger anchor energy will result in greater contact loss. Interestingly, if both mechanical coordination number and relative penetration are normalized by their limiting values for each simulation (Fig. 27(b)), all of the curves presented in Fig. 27(a) collapse. This implies that system response is not only linear at the macroscale for varying anchor weight (i.e., Fig. 12), but also at the microscale, validating our fundamental belief that observable behaviors at the assembly scale are driven directly by system response at the particle scale.

3.3. Energy dissipation

Energy evolution during anchor penetration consists of evaluation of collisional energy dissipation and frictional energy dissipation [23]: anchor energy dissipates in two ways simultaneously. Collisional energy dissipation rate at the particle level can be calculated as:

$$\textit{Collisional energy dissipation rate} = \sum_{c=1}^{N_c} (F_n^V)_c \dot{\delta}_c \tag{8}$$

where $(F_n^V)_c$ is the viscous normal force at contact c, $\dot{\delta}_c$ is associated relative normal velocity between the contacting particles, N_c is the number of contacts. Total collisional energy dissipation is obtained by integrating dissipation rates with time. Frictional energy dissipation rate can be calculated as:

$$\textit{Frictional energy dissipation rate} = \sum_{c=1}^{N_s} \mu_p (F_n)_c |\dot{q}_c| \tag{9}$$

where $(F_n)_c$ is the total normal contact force at contact c, $\dot{q}_c$ is the relative tangential velocity between the contacting particles, N_s is the number of sliding contacts. Total frictional energy dissipation can be obtained similarly to total collisional energy dissipation.

Similar to an intruder impacting soil targets, the impact of a torpedo anchor on seabed soils can generate stress waves that propagate through the soil assembly. Some of the energy is dissipated upon impact on the soil surface through generation of stress waves [23]. The remaining energy is dissipated through frictional, collisional, and potential energy mechanisms [3,23]. Fig. 28 shows the energy dissipation ratio (ED_r) between frictional energy dissipation and collisional energy dissipation during anchor penetration. Results shows that during anchor penetration, energy dissipation through frictional sliding is approximately 6–8 times that through particle collision. The energy

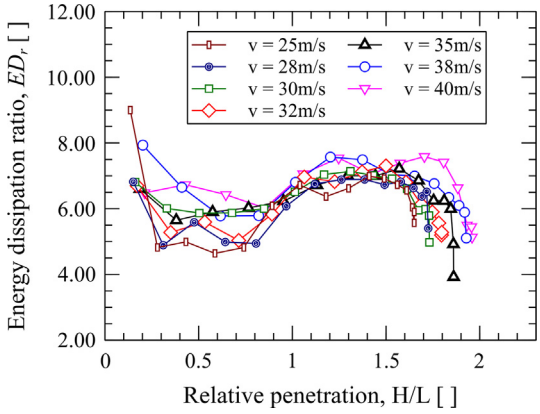

Fig. 28. Energy dissipation during penetration under different impact velocities.

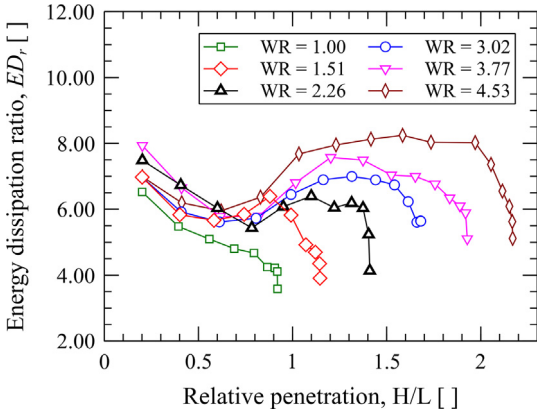

Fig. 29. Energy dissipation during penetration under different anchor weights (v = 38 m/s).

dissipation ratio experiences a decrease, then an increase, followed finally by another decrease. These effects on the energy dissipation ratio are also significant for different anchor weights (Fig. 29) and different interparticle frictions (Fig. 30).

Fig. 29 shows that the stress wave propagation effects are more significant when the anchor weight is larger. According to the Impulse-Momentum Theorem, Newton's Second Law, and the linear force-displacement law, for the same impact velocity the larger the anchor weight, the larger the mean stress. Since frictional energy dissipation is amplified by increasing mean stress, the larger the anchor weight, the

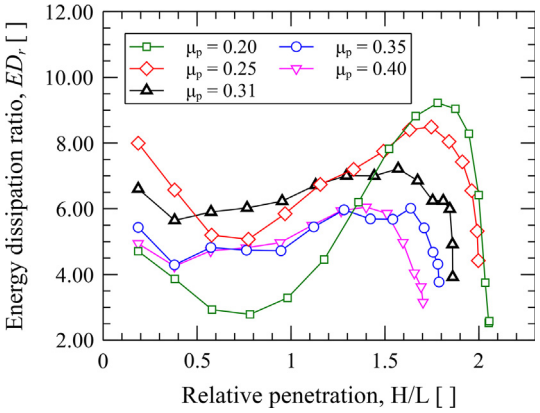

Fig. 30. Energy dissipation during penetration for different interparticle frictions (v = 35 m/s).

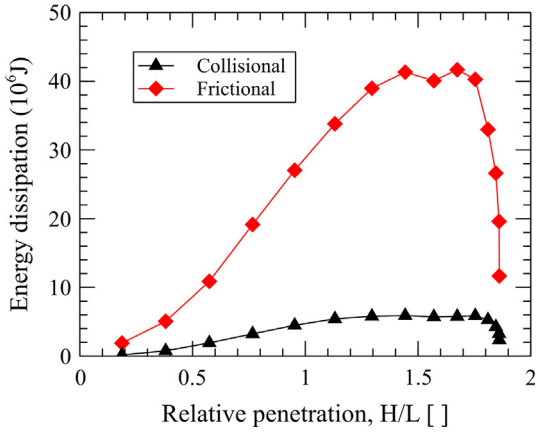

Fig. 31. Diagram of energy dissipation during penetration (v = 35 m/s, μ = 0.31).

larger the energy dissipation ratio. The peak energy dissipation ratio of the heaviest anchor (WR = 4.53) is $ED_r \cong 8$. During further penetration, additional particle displacements occur in the assembly due to significant compression and shearing in a translationally and rotationally frustrated assembly. Shear deformation results in an increase in frictional energy dissipation (Fig. 31) and an increase in frictional energy dissipation ratio (Figs. 28–30). In addition to the energy dissipated through collisional and frictional particle interactions, matrix volume change due to particle sliding, rotation, and climbing over one another also dissipates anchor energy [23].

3.4. Contact force chain

Fig. 32 shows the contact force chain of the granular assembly during (left) and at the end of (right) anchor penetration. Initial anchor penetration primarily influences the particles around the anchor tip. As penetration progresses, anchor penetration influences not only particles at the anchor tip, but also those along the anchor shaft, as shear deformation occurs at the grain-anchor interface. As stressed above, shear deformation occurs at deep penetrations where frictional energy dissipation is significant. As seen in Fig. 32, larger contact forces exist not only on the anchor tip but along the anchor shaft. According to Eq. (7), relative tangential velocity between the grain and the anchor are significant, and energy is dissipated through frictional sliding between particles and at the anchor-grain contacts as the anchor is penetrated.

3.5. Contact force distribution

A cylindrical window with a diameter of $20d_{50}$ surrounding the torpedo anchor is used to calculate the contact normal force distribution. Five different stages of penetration are considered. Fig. 33 shows the probability distribution of contact normal forces at different penetration depths for an impact velocity of 35 m/s. The contact normal forces have been normalized by the mean contact normal force before anchor penetration (i.e., h/L = 0.00). Results show that the range of contact normal forces increases as penetration progresses. However, at the end of penetration (h/L = 1.86) the normalized contact force varies over a narrower range than relative penetration h/L = 1.67 as the system relaxes to static equilibrium.

4. Conclusions

Macro- and microscale analyses of torpedo anchor penetration into granular soils have been presented in this paper. We have considered the effects of both anchor and soil properties (e.g., impact velocity, anchor weight and soil interparticle friction). The results reported in this paper focus primarily on the influence of anchor impact velocity, anchor weight, and soil interparticle friction on penetration depth and the corresponding anchor holding capacity, which is characterized using a dimensionless parameter termed anchor efficiency. Microscale behaviors (e.g., fabric, coordination number, contact force) are considered and used to aid in the interpretation of macroscale observations. The following conclusions may be drawn from the findings presented above:

1. Within the range of impact velocities considered (25–40 m/s), maximum relative penetration depth increases linearly with an increase in impact velocity. Anchor weights are found to influence the maximum penetration in a linear relationship as well. Results show that the larger the anchor weight, the deeper the anchor penetration. The maximum relative penetration depth decreases with increasing interparticle friction.
2. Comparing to published experimental results, relative penetration depth increases linearly with increasing impact velocity at the same rate for OC clays, sands, and DEM simulations. The trends in penetration depth versus anchor impact velocity for these cases are consistent and collectively well-fit by a straight line.
3. Fabric anisotropy near the anchor for all impact velocities considered initially increases slightly and then decreases significantly during anchor installation. A similar trend is observed for different anchor weights. However, if interparticle friction is decreased, fabric anisotropy near the anchor decreases monotonically after initial impact.
4. During penetration, mechanical coordination number near the anchor initially decreases dramatically and then increases as the anchor comes to static equilibrium. Mechanical coordination number in the far field does not change appreciably during anchor penetration. The system response is found not only to be linear at the macroscale for varying anchor weight, but also at the particle scale.
5. Energy dissipation through frictional sliding is approximately 6–8 times higher than that due to particle collisions. Stress wave propagation causes energy dissipation ratio to first decrease, followed by an increase, and then a final decrease as the anchor approaches its final installation depth. This phenomenon is found in all considered cases.
6. At the initial stages of penetration, particles near the anchor tip are most significantly influenced. As penetration proceeds, particles along the anchor shaft become engaged as shear deformation occurs at the grain-anchor interface. Shear deformation occurs at deep penetrations where frictional energy dissipation is significant. The ranges of the magnitudes of contact normal forces are found to increase as penetration progresses. However, at the end of penetration

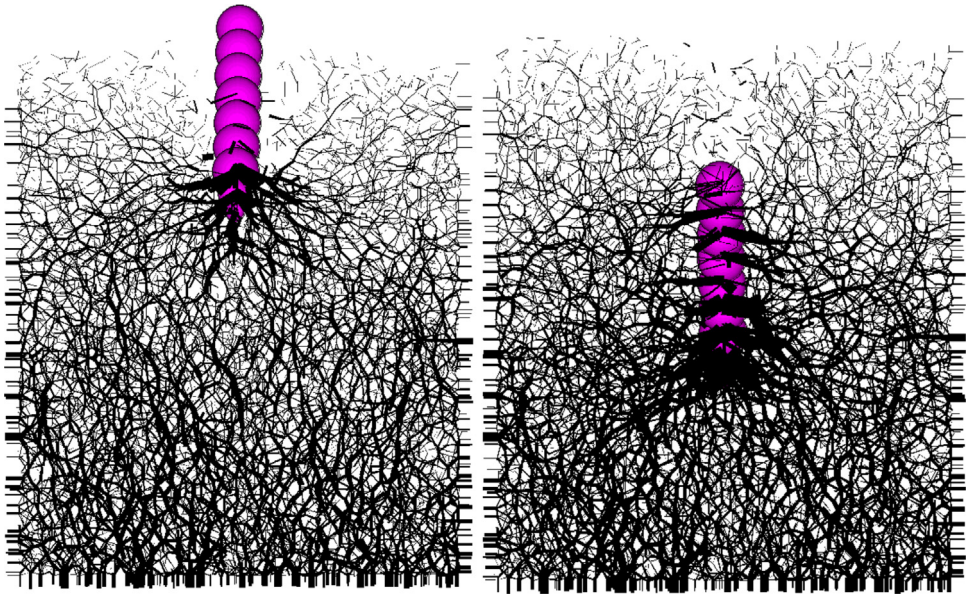

Fig. 32. Contact force chain of the granular assembly in the middle(left) and at the end (right) of penetration (μp = 0.31, v = 35 m/s).

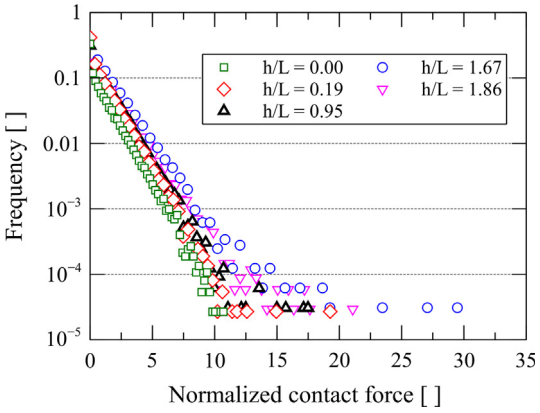

Fig. 33. Probability of contact normal force at different penetration depths (v = 35 m/s).

the normalized contact force varies over a narrower range as the system relaxes to static equilibrium.

Acknowledgement

This material is based upon work supported by the Department of Energy under Award Number DE-FG36-08GO18179. This paper was prepared as an account of work sponsored by an agency of the United States Government. Neither the United States Government nor any agency thereof, nor any of their employees, makes any warranty, expressed or implied, or assumes any legal liability or responsibility for the accuracy, completeness, or usefulness of any information, apparatus, product, or process disclosed, or represents that is use would not infringe privately owned rights. The views and opinions of the authors expressed herein do not necessarily state or reflect those of the United States Government or any agency thereof. We also thank the anonymous reviewers for their valuable comments and suggestions to improve this work.

References

[1] Audibert JM, Movant MN, Jeong-Yun W, Gilbert RB. Torpedo piles: laboratory and field research. The sixteenth international offshore and polar engineering conference. San Francisco (California, USA): International Society of Offshore and Polar Engineers; 2006.
[2] Boguslavskii Y, Drabkin S, Salman A. Analysis of vertical projectile penetration in granular soils. J Phys D Appl Phys 1996;29(3):905.
[3] Braslau D. Partitioning of energy in hypervelocity impact against loose sand targets. J Geophys Res 1970;75(20):3987–99.
[4] Butlanska J, Arroyo M, Gens A, O'Sullivan C. Multi-scale analysis of cone penetration test (CPT) in a virtual calibration chamber. Can Geotech J 2013;51(1):51–66.
[5] Chow SH, O'Loughlin CD, Gaudin C, Knappett JA, Brown MJ, Lieng JT. An experimental study of the embedment of a dynamically installed anchor in sand. Proceedings of the 8th Offshore Site Investigation and Geotechnics Conference (OSIG17), London, UK. 2017. p. 1019–25.
[6] Chow SH, O'Loughlin CD, Gaudin C, Lieng JT. Drained monotonic and cyclic capacity of a dynamically installed plate anchor in sand. Ocean Eng 2018;148:588–601.
[7] Ciantia MO, Arroyo M, Butlanska J, Gens A. DEM modelling of cone penetration tests in a double-porosity crushable granular material. Comput Geotech 2016;73:109–27.
[8] Collins AL, Addiss JW, Walley SM, Promratana K, Bobaru F, Proud WG, et al. The effect of nose shape on the internal flow fields during ballistic penetration of sand. Int J Impact Eng 2011;38:951–63.
[9] Cundall PA, Strack OD. A discrete numerical model for granular assemblies. Geotechnique 1979;29(1):47–65.
[10] Cundall PA. Distinct element models of rock and soil structure. Anal Comput Meth Eng Rock Mech 1987:129–63.
[11] Ehlers CJ, Young AG, Chen JH. Technology assessment of deepwater anchors. In: Offshore technology conference. Houston, Texas, USA; 2004.
[12] El Shamy U, Patsevich A. DEM simulation of the seismic response of gravity retaining walls. In: 6th International conference on earthquake geotechnical engineering, Christchurch, New Zealand; 2015.
[13] Evans TM, Frost JD. Multiscale investigation of shear bands in sand: physical and numerical experiments. Int J Numer Anal Meth Geomech 2010;34(15):1634–50.
[14] Evans TM, Kress JG. Discrete simulations of particulate-structure interactions. ASCE GeoFrontiers 2011, Geotechnical Special Publication No. 211: Advances in Geotechnical Engineering, Dallas, TX; 2011. p. 4252–2.
[15] Evans TM, Zhang N. Three dimensional simulations of plate anchor pullout in granular materials. Int J Geomech 2018. https://doi.org/10.1061/(ASCE)GM.1943-5622.0001367.
[16] Fragaszy RJ, Taylor TA. Centrifuge modeling of projectile penetration in granular soils (NO. ESL-TR-88-76). Pullman: Dept of Civil and Environmental Engineering, Washington State University; 1989.
[17] Freeman TJ, Murray CN, Schuttenhelm RTE. The Tyro 86 penetrator experiments at Great Meteor East. In: Oceanology'88: Proceedings of an international conference. Society of Underwater Technology, Brighton, UK; 1988.
[18] Frost JD, Hebeler GL, Evans TM, DeJong JT. Interface behavior of granular soils. Proceedings of the 9th ASCE aerospace division international conference on engineering, construction, and operations in challenging environments, Houston, TX, USA. 2004. p. 65–72.
[19] Frost JD, Evans TM, Lu Y, Zhao X. Selected observations from 3-D experimental and numerical studies of shear banding in biaxial shear tests. ASCE geo-congress 2012, Geotechnical special publication no. 225: state of the art and practice in geotechnical engineering, Oakland, CA; 2012. p. 1116–25.
[20] Gao G, Meguid MA. Modeling the impact of a falling rock cluster on rigid structures. Int J Geomech 2017;18(2):04017141.

[21] Hossain MS, O'Loughlin CD, Kim Y. Dynamic installation and monotonic pullout of a torpedo anchor in calcareous silt. Géotechnique 2015;65(2):77–90.
[22] Hou M, Peng Z, Liu R, Wu Y, Tian Y, Lu K, et al. Projectile impact and penetration in loose granular bed. Sci Technol Adv Mater 2005;6(7):855.
[23] Iskander M, Bless S, Omidvar M. Rapid penetration into granular media: visualizing the fundamental physics of rapid earth penetration. NYC, NY, USA: Elsevier; 2015.
[24] Itasca Consulting Group. (2008). PFC3D: Particle flow code in three dimensions v4. 0. Minneapolis, MN.
[25] Jacobson DE, Valdes JR, Evans TM. A numerical view into direct shear specimen size effects. ASTM Geotech Test J 2007;30(6):512–6.
[26] Jensen RP, Edil TB, Bosscher PJ, Plesha ME, Kahla NB. Effect of particle shape on interface behavior of DEM-simulated granular materials. Int J Geomech 2001;1(1):1–19.
[27] Jensen RP, Plesha ME, Edil TB, Bosscher PJ, Kahla NB. DEM simulation of particle damage in granular media—structure interfaces. Int J Geomech 2001;1(1):21–39.
[28] Kim Y, Hossain MS, Wang D. Numerical modelling of dynamic installation of a torpedo anchor in calcareous silt. In: The twenty-fourth international ocean and polar engineering conference. International Society of Offshore and Polar Engineers, Busan, South Korea; 2014.
[29] Kress JG, Evans TM. Analysis of pile behavior in granular soils using DEM. Proceedings of the 35th annual deep foundations institute annual conference, Hollywood, CA. 2010.
[30] Lieng JT, Hove F, Tjelta TI. Deep penetrating anchor: subseabed deepwater anchor concept for floaters and other installations. In: The ninth international offshore and polar engineering conference. International Society of Offshore and Polar Engineers, Brest, France; 1999.
[31] Lieng JT, Kavli A, Tjelta TI. Deep penetrating anchor: further development, optimization and capacity clarification. In: Presented at the 10th international offshore and polar engineering conference. International Society of Offshore and Polar Engineers; 2000.
[32] Medeiros Jr CJ. Low cost anchor system for flexible risers in deep waters. In: Offshore technology conference. Houston, TX, USA; 2002. doi: 10.4043/14151-MS.
[33] O'Beirne C, O'Loughlin CD, Wang D, Gaudin C. Capacity of dynamically installed anchors as assessed through field testing and three-dimensional large-deformation finite element analyses. Can Geotech J 2015;52(5):548–62.
[34] O'Loughlin CD, Randolph MF, Richardson M. Experimental and theoretical studies of deep penetrating anchors. In: Offshore technology conference, Houston, TX, USA; 2004.
[35] O'Loughlin CD, Richardson MD, Randolph MF. Centrifuge tests on dynamically installed anchors. In: ASME 2009 28th International Conference on Ocean, Offshore and Arctic Engineering (pp. 391–399). American Society of Mechanical Engineers, Honolulu, Hawaii, USA; 2009.
[36] O'Loughlin C, Richardson MD, Randolph MF, Gaudin C. Penetration of dynamically installed anchors in clay. Géotechnique 2013;63(11):909–19.
[37] O'Loughlin CD, Blake AP, Richardson MD, Randolph MF, Gaudin C. Installation and capacity of dynamically embedded plate anchors as assessed through centrifuge tests. Ocean Eng 2014;88:204–13.
[38] Potyondy DO, Cundall PA. A bonded-particle model for rock. Int J Rock Mech Min Sci 2004;41(8):1329–64.
[39] Pyrz AP. Gravity effects on low velocity penetration of a projectile into a cohesionless medium (No. GSF/MC/69-6). MS Thesis. Air Force Institute of Tsechnology, Wright-Patterson AFB, OH; 1969.
[40] Raie MS, Tassoulas JL. Installation of torpedo anchors: numerical modeling. J Geotech Geoenviron Eng 2009;135(12):1805–13.
[41] Richardson MD, O'Loughlin CD, Randolph MF. The geotechnical performance of deep penetrating anchors in calcareous sand. Proceedings of the International Symposium on Frontiers in Offshore Geotechnics (ISFOG), Perth. 2005. p. 357–63.
[42] Richardson MD. Dynamically installed anchors for floating offshore structures. Doctoral dissertation, University of Western Australia, Perth, Australia; 2008.
[43] Richardson MD, O'Loughlin CD, Randolph MF, Gaudin C. Setup following installation of dynamic anchors in normally consolidated clay. J Geotech Geoenviron Eng 2009;135(4):487–96.
[45] Shahin MA, Jaksa MB. Pullout capacity of small ground anchors by direct cone penetration test methods and neural networks. Can Geotech J 2006;43(6):626–37.
[46] Taylor T, Fragaszy RJ, Ho CL. Projectile penetration in granular soils. J Geotech Eng 1991;117(4):658–72.
[47] Thornton C. Quasi-static simulations of compact polydisperse particle systems. Particuology 2010;8(2):119–26.
[48] Thornton C, Antony SJ. Quasi-static deformation of particulate media. Philos Trans R Soc Lond, Series A 1998;356:2763–82.
[49] True DG. Penetration of projectiles into seafloor soils (No. CEL-TR-822). Civil Engineering LAB (NAVY). Port Hueneme CA; 1975.
[50] Van Der Meer D. Impact on granular beds. Annu Rev Fluid Mech 2017;49:463–84.
[51] Van Vooren A, Borg J, Sandusky H, Felts J. Sand penetration: a near nose investigation of a sand penetration event. Procedia Eng 2013;58:601–7.
[52] White DJ, O'Loughlin CD, Stark N, Chow SH. Free fall penetrometer tests in sand: determining the equivalent static resistance. In: CPT18-4th international symposium on cone penetration testing, Delft, NL; 2018. p. 695–701.
[53] Wang WL. Experimental study of projectile penetration in Ottawa sand at low velocities. J Spacecraft Rockets 1969;6(4):497–8.
[54] Wang WL. Low velocity projectile penetration. J Soil Mech Found Divis 1971;97(12):1635–55.
[55] Yun G, Bransby MF. The undrained vertical bearing capacity of skirted foundations. Soils Found 2007;47(3):493–505.
[56] Zamani N, El Shamy U. Analysis of the seismic response of soil–foundation–structure systems using a microscale framework. Soil Dyn Earthquake Eng 2012;43:398–412.
[57] Zhang N, Evans TM. Towards anchoring of marine hydrokinetic energy devices: three dimensional discrete element method simulations of interface shear. In: GeoChicago; 2016. p. 503–12.
[58] Zhang N, Evans TM. Offshore anchor penetration in sands—granular simulations. In: Geotechnical frontiers; 2017. p. 132–42.
[59] Zhang N, Evans T Matthew. Three dimensional discrete element method simulations of interface shear. Soils Found 2018;58(4):941–56.
[60] Zhao X, Evans TM. Discrete simulations of laboratory loading conditions. Int J Geomech 2009;9(4):169–78.
[61] Zhao X, Evans TM. Numerical analysis of critical state behaviors of granular soils under different loading conditions. Granular Matter 2011;13(6):751–64.
[62] Zhao S, Evans TM, Zhou X. Effects of curvature-related DEM contact model on the macro-and micro-mechanical behaviours of granular soils. Géotechnique 2018;17:158.
[63] Zhao S, Evans TM, Zhou X. Shear-induced anisotropy of granular materials with rolling resistance and particle shape effects. Int J Solids Struct 2018;150:268–81.
[64] Zhao S, Zhang N, Zhou X, Zhang L. Particle shape effects on fabric of granular random packing. Powder Technol 2017;310:175–86.
[65] True DG. Undrained vertical penetration into ocean bottom soils. Berkeley, CA, USA: University of California; 1976. PhD thesis.
[66] Lieng Jon Tore, Kavli Arne, Hove Frode, Tjelta Tot Inge. Deep penetrating anchor: further development, optimization and capacity verification. In: The tenth international offshore and polar engineering conference. International Society of Offshore and Polar Engineers; 2000.
[67] True DG. Rapid penetration into seafloor soils. In: Proceedings of offshore technology conference. Houston, OTC2095; 1974.
[68] Jiang MJ, Yu H-S, Harris D. Discrete element modelling of deep penetration in granular soils. Int J Numer Anal Methods Geomech 2006;30(4):335–61.
[69] Dove JE, Bents DD, Wang J, Gao B. Particle-scale surface interactions of non-dilative interface systems. Geotext Geomembr 2006;24(3):156–68.
[70] Belheine N, Plassiard J-P, Donzé F-V, Darve F, Seridi A. Numerical simulation of drained triaxial test using 3D discrete element modeling. Comput Geotech 2009;36(1–2):320–31.
[71] Barreto D. Numerical and experimental investigation into the behaviour of granular materials under generalised stress states, Ph.D. thesis. Imperial College London; 2010.
[72] O'Sullivan C. Particulate discrete element modelling: a geomechanics perspective. London: Spon; 2011.

Further reading

[44] Salot C, Gotteland P, Villard P. Influence of relative density on granular materials behavior: DEM simulations of triaxial tests. Granular Matter 2009;11(4):221–36.